Catalysis Science & Technology

Accepted Manuscript

ROYAL SOCIETY OF CHEMISTRY

www.rsc.org/catalysis

Catalysis Science & Technology

ARTICLE

Importance of porous structure and synergistic effect on the catalytic oxidation activities over hierarchical Mn-Ni composite oxides

Received 00th January 20xx,
Accepted 00th January 20xx

DOI: 10.1039/x0xx00000x

www.rsc.org/

Wenxiang Tang [a,b], Yuzhou Deng [a], Wenhui Li [a], Jiaqi Li [a], Gang Liu [a], Shuangde Li [a], Xiaofeng Wu [a*], Yunfa Chen [a*]

The hierachically porous manganese-nickel composite oxides (MNCOs) were successfully synthesized by an oxalate route and further applied for catalytic removal of benzene. Among these catalysts, the best one was Mn_2Ni_1 mixed oxide which exhibited uniform hierarchical lithops-like topography, rich porous structure and high surface area of 201.1 m^2 g^{-1}. The temperature required for benzene conversion of 90% over this catalyst was ca. 232 °C under the condition of benzene concentration of 1000 ppm in air and high space velocity of 120,000 mL g^{-1} h^{-1}, which was 54 ºC lower than that on the non-porous MNCO particles prepared by a traditional approach. The reaction kinetic study showed the apparent activation energies (45.2 kJ mol^{-1}) for total oxidation of benzene over the Mn_2Ni_1 oxide catalyst were much lower than those (72.4-97.2 kJ mol^{-1}) over other catalysts. With XPS and H_2-TPR analysis, the porous MNCOs own higher content of surface-adsorbed oxygen species and better low-temperature reducibility which can be ascribed to a possible synergetic effect between Mn and Ni ions in the spinel mixed oxides.

1.0 Introduction

In the past few years, haze has become a serious environmental issue in many developing countries like China[1, 2] and volatile organic compounds (VOCs) emitted from many industrial processes make major contribution on the formation of photochemical smog and ozone pollution[3, 4]. Meanwhile inhalation exposure of VOCs can induce a range of adverse human health effects such as headache, respiratory irritation, skin irritation and even cancer[5, 6]. Moreover, Sick building syndrome (SBS) has been wide spread in many families because of the toxic VOCs in poor indoor environment, even if at very low concentration. Compared to the traditional techniques such as adsorption and high-temperature combustion for elimination of VOCs, catalytic oxidation is recognized as a perfect way requiring temperatures ca. 300-600 ºC by which the toxic organics can be converted into benign products without any risks[7, 8]. For the deep oxidation of VOCs, noble metals as Pd and Pt[9, 10] catalysts show high activities and have been used in some industrial processes. However, more general application is limited in many fields because of their low availability, easily sintering/coking, and high cost problems.

Therefore, people now focused on substitution of precious metals catalysts with bulk and supported metal oxides (MnO_x, Co_3O_4, NiO, CeO_2 etc)[11-13] which were found to be active for oxidation of VOCs. For an example, manganese oxides such as MnO_2 and Mn_2O_3 were selected as environmental friendly catalysts for catalytic removal of many hydrocarbons because of their reversible redox couples like Mn^{4+}/Mn^{3+} and Mn^{3+}/Mn^{2+}. The unique redox properties are good for making use of surface oxygen and activating gaseous oxygen during the catalytic oxidation process. Gandhe et al.[14] presented that cryptomelane type octahedral molecular sieve catalyst was very active for total oxidation of ethyl acetate, in which the presence of Mn^{4+}/Mn^{3+} type redox couples and facile lattice oxygen on the catalysts were the main contributors. Besides, Co_3O_4 and NiO are also known as active components for catalytic oxidation of toluene[15], 1,2-dichloroethane[16] etc. Developing the non-noble metal catalysts may be beneficial to getting high active catalysts for total oxidation of VOCs.

However, the single oxides usually may not perform very well in catalytic oxidation of VOCs so that many efforts are made to improve their activities. The first effective way is of introducing another component into a single oxide to form mixed oxides in which the synergistic effects enhance their catalytic activities significantly. This promoting effect has been found to be present in many composite oxides such as Co-Ce-O[17], Cu-Ce-O[18], Mn-Ce-O[19], Ce-Zr-O[20-22] and Mn-Co-O[23-25] systems. Moreover, building a novel porous nanostructure gives another efficient pathway to develop highly active metal oxide catalysts. Previously, we reported a co-nanocasting method for

[a], Institute of Process Engineering, Chinese Academy of Sciences, Beijing 100190, China. E-mail: chenyf@ ipe.ac.cn & wxftsjc@ipe.ac.cn; Fax: +86 10 8254 4896; Tel: +86 10 8254 4896
[b] Institute of Materials Science, University of Connecticut, Storrs 06269-3136, USA.
† Footnotes relating to the title and/or authors should appear here.
Electronic Supplementary Information (ESI) available: [details of any supplementary information available should be included here]. See DOI: 10.1039/x0xx00000x

producing mesoporous Cu-Mn mixed oxides with high surface areas which displayed superior catalytic activity[26].

Among the general metal oxides, transitional oxides like manganese oxide or nickel oxide with low cost and good reducibility have turned out to be a kind of high efficient catalysts for total oxidation of VOCs [12, 27] and selective reduction[28]. In this work, a facile oxalate approach was applied to fabricate a series of manganese-nickel mixed oxides (MNCOs) involving preparation of binary Mn-Ni oxalate precursors followed by a pyrolysis process. A well-developed porous structure can be created during the decomposition of oxalate precursors and solid solution oxides were successfully obtained. As a carcinogenic VOC, benzene is widely used in many chemical industries such as chemical synthesis, petrochemical process and paintings. Herein, benzene is used as a target toxic gas for testing the catalytic activity of as-prepared materials. Over the best catalyst, the temperature acquiring for benzene conversion of 90% can be low to ca. 232 °C at a high space velocity = 120,000 mL g^{-1} h^{-1}. It can be found that the nature of texture properties such as surface area, reducibility and active oxygen species were significantly enhanced by the synergetic effect created in MNCOs, which makes a great contribution on the superior catalytic activities. The long-term and water-resistance test showed the good performance of prepared catalysts that will be easy to get a practical application in the future. Moreover, the vital role of porous structure in catalytic oxidation reaction was proved by comparing the catalytic performances of porous and nonporous structured MNCOs.

2.0 Experimental

2.1 Synthesis of Catalysts

2.1.1 Porous Mn-Ni mixed oxides

A series of Mn-Ni mixed oxides were prepared by an oxalate route, following the similar procedures as described in our previous study[23]. Typically, 50 ml aqueous solution with 24 mmol $H_2C_2O_4$ was added directly into another 150 ml solution containing a total of 20 mmol metal ions (Mn^{2+}, Ni^{2+} or mixed) under strong stirring at room temperature. The mixed solution was stirred for 30 min and further aged for 12 h under a static condition. The suspension was then filtered, washed with deionized water, and dried in an oven at 80 °C overnight. The as-prepared samples were treated for 4 h at 450 °C in air atmosphere with a temperature ramp of 5 °C min^{-1}. The different experimental Mn^{2+}/Ni^{2+} mole ratios were set at 1/0, 2/1, 1/1, 1/2, 0/1, and the related samples were denoted as Mn, Mn_2Ni_1, Mn_1Ni_1, Mn_1Ni_2, Ni, respectively.

2.1.2 Porous Mn-Ni mixed oxides

A general nonporous Mn-Ni composite oxide with optimal ratio was fabricated by a traditional co-precipitation with NaOH solution as a precipitant. Typically, an excess of NaOH solution was added in another solution containing mixed metal ions (Mn^{2+} and Ni^{2+}) under vigorous stirring at room temperature and the final pH was about 10.0. After stirring for 30 min, the suspension was aged for 12 h. The following procedures such as filtering, washing, drying and calcination were similar to the synthesis of porous mixed oxides described before.

2.2 Characterization

The crystal structures of as-prepared catalysts were analyzed by X-ray powder diffraction (XRD) method with a Panalytical X'Pert PRO system using Cu-Kα radiation in the diffraction angle (2θ) range 5-90° at a scan rate of 15 ° min^{-1}. The crystallite sizes of all samples were calculated by Scherrer equation using full-width half-maximum (FWHF) of the strongest diffraction peaks. The BET surface areas were determined via N_2 adsorption at -196 ºC on an automatic surface analyzer (SSA-7300, China), and Barrett-Joyner-Halenda (BJH) method was used to calculate the pore-size distributions. All samples were pre-degassed at 150 °C for 5 h under vacuum condition before each experiment. The structural properties were obtained on a scanning electron microscopy (SEM, JEOL JSM-7001F) and a transmission electron microscopy (TEM, JEOL JEM-2010F). Hydrogen temperature programmed reduction (H_2-TPR) was used to determine the reducibility of the catalysts, which was performed in a U-shaped quartz reactor under a gas flow (5% H_2 balanced with Ar, 25 mL min^{-1}) with an automated catalyst characterization system (Autochem 2920, Micromeritics). About 30 mg catalyst (40~60 mesh) was loaded in every test and the temperature was raised to 700 °C from room temperature at a constant rate 10 °C min^{-1}. Surface composition of the samples were collected by X-ray photoelectron spectroscopy (XPS) method which was performed on a XLESCALAB 250Xi electron spectrometer from VG Scientific. The obtained spectra was referenced to the carbon 1s peak at 284.6 eV.

2.3 Catalytic activity testing

A conventional U-shaped fixed bed quartz microreactor (i.d. 6 mm) was used for catalytic activity tests which has been described in details elsewhere[23, 26]. Typically, 50 mg catalyst (mesh 40-60) mixed with 300 mg of quartz sands (mesh 40-60) was loaded in the reactor with quartz wool packed and the reaction temperature was continuously detected by a thermocouple inside the furnace. The reactant gas was composed of 1000 ppm benzene in synthetic air from gas cylinder which was bought from Beijing Huayuan Co. and the weight hourly space velocity (WHSV) was typically set at 120, 000 mL g^{-1} h^{-1}. The reactants and products (C_6H_6, CO and CO_2) were analyzed by a gas chromatograph (Shimadzu GC-2014) equipped with two flame ionization detectors (FID) and a thermal conductivity detector (TCD). A capillary column (Stabilwax-DA 0.53 mm×0.5 μm×30 m) and a FID were applied to separate and detect gaseous benzene. A Porapak-N column (80/100 mesh 1.0 m×3.2 mm×2.1 mm) and a FID with a conversion furnace for converting CO_2 to CH_4 was employed to separate and measure low concentration of CO_x. Carbon balance was above 99.5% in each run. The test of moisture-resistant property was carried out in the presence and absence of 1.5 vol% water vapor at a certain temperature during an on-stream VOCs oxidation experiment.

In the presence of excess oxygen, the complete oxidation of VOCs such as benzene[29], toluene[29], propane[30] and ethyl acetate[29] can obey the first-order reaction which was also discussed in our previous study[26]. Therefore, it can be reasonably supposed that the total oxidation of VOCs molecules in the presence of rich oxygen (the mole ratio of oxygen/VOC is above 200) would obey a reaction mechanism: $\gamma = (A \exp(-E_a/RT))$ which is equal to $\ln \gamma = -Ea / (RT) + C$, where the γ, A and E_a are the reaction rate, the pre-exponential factor and the apparent activation energy (kJ mol^{-1}), respectively. The kinetics testing was operated in the fixed-bed reactor for benzene oxidation as above-mentioned and every experimental point was achieved at a benzene conversion below 15% after the reaction was stable for at least 60 min.

3.0 Results and discussion

3.1 Catalytic performance

As shown in Figure 1, the light-off curves for benzene oxidation were obtained as a function of temperature 100-400 ºC. For the single oxides, manganese oxide exhibited significantly higher activity than nickel oxide, and the total oxidation of benzene took place close to 300 ºC over the manganese oxide while the value was above 400 ºC over the nickel oxide. In contrast with the pure oxides, the incorporation of nickel element into the manganese oxides enhanced catalytic activity towards benzene oxidation. The efficiency increased in the order: $Mn_2Ni_1 > Mn_1Ni_1 > Mn_1Ni_2 \approx Mn > Ni$. The lowest oxidation temperature was observed on Mn_2Ni_1, which showed a significant higher activity with respect to pure oxides and remaining mixed oxides. The reaction temperatures for benzene conversion of 10% ($T_{10\%}$), 50% ($T_{50\%}$) and 90% ($T_{90\%}$) are summarized in Table 1. Apparently, the $T_{10\%}$, $T_{50\%}$, $T_{90\%}$ values of the Mn_2Ni_1 catalyst were 179, 212 and 232 ºC for benzene oxidation, respectively, which are 21, 29 and 41 ºC lower than those over single manganese oxide and 93, 117 and 147 ºC lower than those over single nickel oxide. The catalytic oxidative activities towards benzene of different mixed oxide catalysts in previous literatures are also listed in Table S1. Although the higher space velocity (120,000 mL g^{-1} h^{-1}) used in this study, the performance achieved here is far better than the reported results, even that of the typical precious metal catalysts. Moreover, a general MNCO prepared by a NaOH co-precipitation method was also used for catalytic removal of benzene and the result was displayed in Figure 1b. The $T_{90\%}$ achieved over the NaOH-derived MNCO particles was 286 ºC which was 54 ºC higher than that on the oxalated-derived MNCO particles. Meanwhile, the reaction rate at 250 ºC over the porous Mn_2Ni_1 particle was 14.75×10^{-2} mol g_{cat}^{-1} s^{-1} which was three times higher than that of general sample, further indicating the oxalate-derived materials have a great competitive advantage.

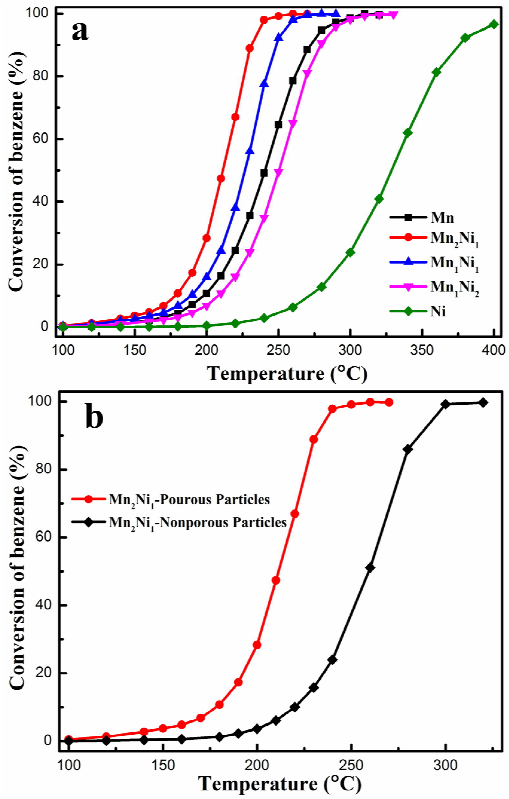

Fig. 1. C_6H_6 conversion over the MNCO catalysts (a, oxalate-derived samples; b, porous and non-porous Mn_2Ni_1 samples) as a function of temperature.

Many publications have confirmed that the catalytic oxidation of VOCs including benzene, toluene, propane and ethyl acetate obeys a first-order reaction kinetic mechanism [26, 29, 30]. Fig. 2 displays the linear Arrhenius plots of the MNCO catalysts for benzene oxidation with conversion < 15%. The related Ea values were calculated by using the slopes of the Arrhenius plots and the results are shown in Table 1. The correlation coefficients (R^2) were rather close to 1.0 which demonstrated the excellent linear relationships of ln(r) versus 1000/T for all catalysts. The related Ea values could be estimated according to the slopes of the Arrhenius plots and the results were shown in Table 1. It is observed that the Ea values of the single manganese and nickel oxide catalysts (79.2 and 88.6 kJ mol^{-1}) were much higher than those (45.2-88.6 kJ mol^{-1}) of the MNCO catalysts. These results support the surface reaction kinetics of MNCO catalysts is higher than the single manganese oxide or nickel oxide catalysts, and the Mn_2Ni_1 catalyst possesses the lowest apparent activation energy of 45.2 KJ.mol^{-1}. Compared to the value (97.2 kJ mol^{-1}) obtained on non-porous MNCO catalyst, the oxalate-derived porous sample possessed a much lower value clearly.

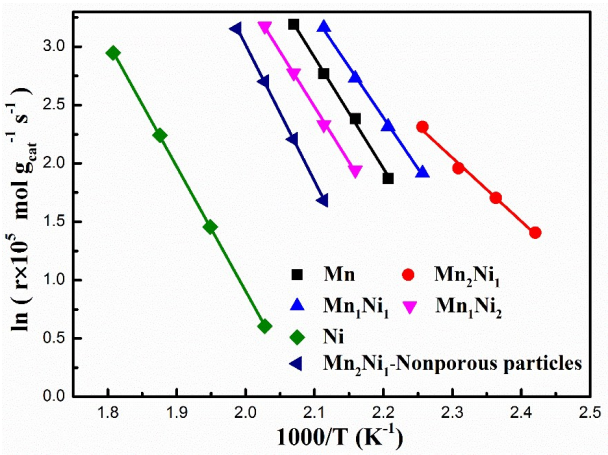

Fig. 2. Arrhenius plots (ln (r × 10^5 mol gcat^{-1} s^{-1}) vs 1000/T (K^{-1})) for total oxidation of benzene over the MNCO catalyst.

From the viewpoint of practical perspective, the stability and water-resistant properties of catalysts are important issues which need to be tackled. Figure 3 shows the result of on-stream benzene oxidation experiments at a constant temperature (250 ºC) in the presence and absence of 1.5 vol% water vapor. With the as-prepared oxalate-derived catalyst, it is found that no obvious drop was observed in catalytic oxidation of benzene during the first 12 h of on-stream reaction. Remarkably, there was no activity loss in benzene oxidation when 1.5 vol% water vapor was introduced during the second 12 h reaction, and the conversion will be kept constant when the water vapor was cut off. These results reveal the excellent stability and moisture-resistant performance of MNCO catalysts in this study, and better than the reported porous Mn-Cu mixed oxides [26]. Therefore, the oxalate-derived MNCO catalyst was catalytically durable in the high humidity condition and it can be used as promising candidate for practical VOCs oxidation.

Table 1. $T_{10\%}$, $T_{50\%}$, $T_{90\%}$, Reaction Rates (r) at 250°C and Activation Energies (Ea) of MNCO Catalysts for benzene oxidation.

Sample	$T_{10\%}$ (°C)	$T_{50\%}$ (°C)	$T_{90\%}$ (°C)	Reaction rate at 250 °C (× 10^{-2} mol gcat^{-1} s^{-1})	Ea (kJ mol^{-1})	R^2
Mn	200	241	273	9.60	79.2	0.997
Mn_2Ni_1	179	212	232	14.75	45.2	0.991
Mn_1Ni_1	191	228	249	13.71	72.4	0.997
Mn_1Ni_2	210	250	280	7.37	78.6	0.998
Ni	272	329	379	0.63	88.6	0.999
Nonporous Mn_2Ni_1	220	260	286	5.54	97.2	0.999

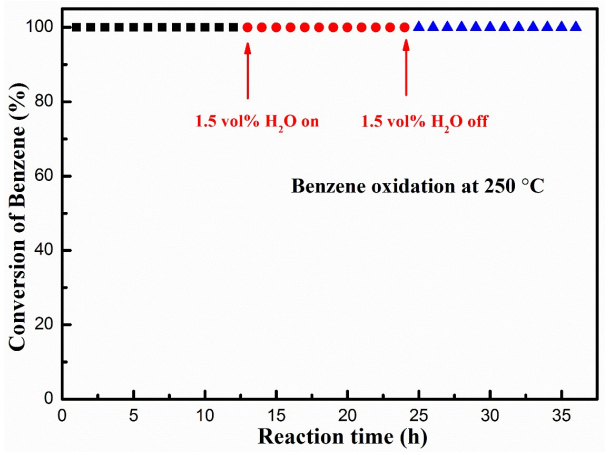

Fig. 3 On-stream benzene oxidation experiments over porous MNCO catalyst (Mn_2Ni_1) at 250 ºC. Benzene concentration= 500 ppm, water concentration = 1.5 vol% and SV = 120,000 mL g^{-1} h^{-1}.

3.2 Structure, morphology and surface properties

3.2.1 XRD and BET analysis

The crystalline phases of as-prepared MNCO samples and pure oxides were determined by the wide-angle XRD patterns which was shown in Figure 4. For single nickel oxide, the sharp diffraction peaks at 2θ=37.2º, 43.3º, 62.9º, 75.4º and 79.4º can be perfectly indexed to the (111), (200), (220), (311) and (222) crystal planes of spinel NiO (JCPDS 47-1049). Whereas the oxalate-derived manganese oxide exhibited complex crystal structure which can be indexed to crystalline Mn_2O_3 (JCPDS 89-4836) and Mn_3O_4 (JCPDS 16-0350) as displayed in Figure 4. With the decomposition of oxalate precursor at 450 ºC, a certain amount of CO_x product could be released[31], and is favorable to generate various manganese oxides with mixed Mn valence. However, all reflections of mixed oxides (Mn_2Ni_1, Mn_1Ni_1 and Mn_1Ni_2) were similar to single nickel oxide, indicating that the spinel solid oxides with different Mn/Ni ratio were formed, like $Mn_2Ni_1O_4$ (JCPDS 01-1110) and $Mn_1Ni_2O_4$ (JCPDS 36-0083). Compared with the single oxides (MnOx and NiO), MNCOs presented wider diffraction peaks with lower intensity, demonstrating the smaller crystal size of mixed oxides. The crystal sizes of as-prepared samples can be calculated by Scherrer equation with strongest peaks from XRD patterns and the results are listed in Table 2. Much smaller crystal sizes were obtained on the MNCO samples, indicating the grain growth of mixed oxides was restrained by the

formation of solid solution compounds. Because of the nano-effect, there will be more active sites on the mixed oxides with smaller sizes so that their activities will be better, which is well consistent with the enhanced catalytic performances of MNCO catalysts. Compared to the porous oxalate-derived MNCO catalyst, the general MNCO particles prepared by traditional method showed similar diffraction peaks (Fig. S1a) with low intensity, which means the solid oxide can also be created by this way but with low crystallinity even mere amorphous structure.. All the as-prepared samples were treated at a same temperature (450 ºC) in air, but only oxalate-derived particles exhibited high degree of crystallinity which would be benefit for keeping stable structure during the catalytic process.

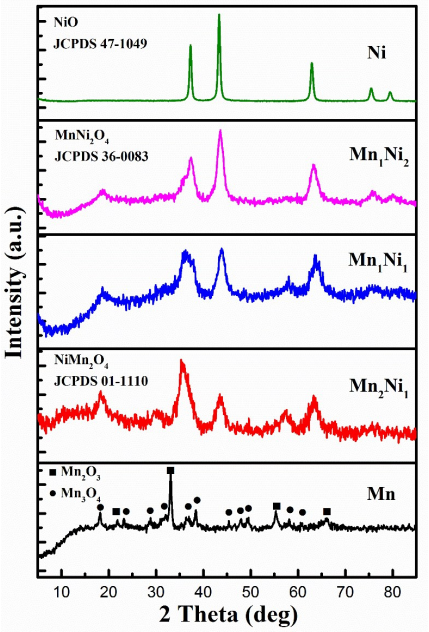

Fig. 4. XRD patterns of oxalate-derived MNCO catalysts.

Table 2 Physical properties (porous structure and crystal size) of MNCO catalys ts.

Sample	Surface area ($m^2 \cdot g^{-1}$)	Pore size (nm)	Pore volume ($cm^3\ g^{-1}$)	D[a] (nm)
Mn	52.6	9.3	0.23	31.4
Mn_2Ni_1	201.1	4.9	0.31	7.4
Mn_1Ni_1	175.5	4.9	0.28	8.5
Mn_1Ni_2	112.6	5.6	0.23	9.3
Ni	27.2	7.8	0.09	16.7
Mn_2Ni_1-nonporous	19.0	85.0	0.25	-

[a]Data calculated based on the XRD results according to the Scherrer equation

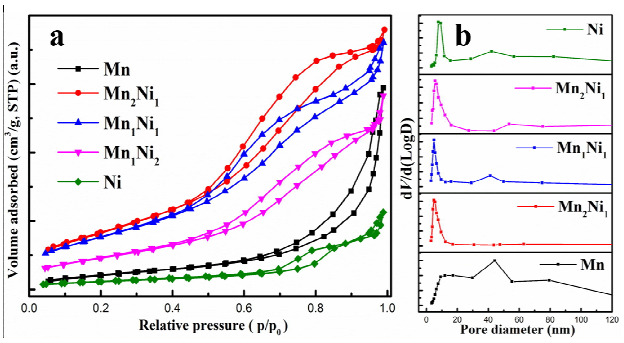

Fig. 5. N_2 adsorption-desorption isotherms and BJH pore-size distribution of the oxalate-derived MNCO catalysts.

The porosity of the as-synthesized MNCOs was also investigated and shown in Figure 5. The N_2 adsorption-desorption isotherms in Figure 5a reveal that the typical IV type characteristics with well-developed H1 type hysteresis loops in the relative pressure range of 0.4-1.0 for the MNCO catalysts, demonstrating the capillary condensation in mesopores and the presence of mesoporous structure within MNCO catalysts. In contrast, the pure MnOx and NiO present the small hystereris loops, revealing the decreasing porosity. The pore size distributions were represented in Figure S1b and the MNCOs and NiO showed noticeable pore size distributions at about 4.9-7.8 nm, different from the bigger pore and wider pore distribution of pure MnOx in macroporous range. As summarized in Table 2, the specific surface area of sample Mn_2Ni_1 is 201.1 $m^2\ g^{-1}$ while the value of single MnO_x and NiO are only 52.6 and 27.2 $m^2\ g^{-1}$. Also, the mixed oxide samples have smaller pore size, further indicating the formation of solid solution oxide is beneficial for developing rich porous structures. Figure S1c displayed the different N_2 adsorption-desorption properties of Mn_2Ni_1 mixed oxide particles synthesized by different methods. There was no obvious hysteresis loops for NaOH-derived sample which might be ascribed to the absence of mesoporous structure and the average pore diameter was high to several dozens of nanometers which would be assigned to the space of the inter-particles.

3.2.2 SEM and TEM results

Figure 6 gives the SEM images of as-synthesized MNCO catalysts. As seen from the SEM images, single manganese oxide exhibits an anomalous feature and single nickel oxide shows spherical morphology. In detail, with the nickel elements introduced, the morphology of products firstly change into lithops-like structures (~3 μm in diameter) when the Mn/Ni ratio was 2:1, then into cubic and spherical particles when the Mn/Ni ratio reached at 1:1 and 1:2, separately. These observations reveals that the Mn/Ni mole ratio plays a vital role in breeding different morphologies of MNCO samples. Moreover, SEM-EDX mapping and TEM elemental mapping analysis was applied to identify the element dispersion of mixed oxides as displayed in Fig. 7 and Fig. S2. It can be seen that both SEM and TEM elemental mapping of the typical Mn_2Ni_1 mixed oxide gives a uniform distribution of Mn, Ni and O in the uniform lithops-like particles and the related peaks can

be found in the spectrum. The uniform element distribution can also demonstrate the formation of solid solution compounds in the MNCO samples. The atomic ratio of Mn/Ni from spectra data is close to 2:1 (initial proportion of raw materials), which can be associated with the complete co-precipitation of initial metal salt solution. The other unsigned peaks in the spectrum of SEM-EDX were Al and Pt which came from the aluminum foils (for dispersing sample) and spray coating Pt (for creating a conductive layer).

The microstructures of the oxalate-derived MNCO and NaOH-derived MNCO catalysts were further observed by HRTEM analysis. As shown in Fig. 8 a1-a3, a typical lithops-like aggregates with clear mesoporous structure can be seen on the oxalate-derived sample which is consistent with the BET results, and the size of disordered pores is lower than 10 nm, which is originated from the decomposition of oxalate chains chelated in the precursors, producing a large amount of voids due to the release of CO_x and H_2O [23]. The lithops-like aggregates are composed of numerous nanoparticles with diameters smaller than 10 nm, in well agreement with the XRD data by Scherrer's equation. Meanwhile, the particle size of NaOH-derived sample (Fig. 8 b1-b3) is above 100 nm and presents non-porous feature except obvious agglomeration. From the high-resolution HRTEM images, two identical intraplanar spacings on each sample were measured to be 0.48 nm and 0.25 nm which can be ascribed to the (111) and (311) crystal phase of the spinel $NiMn_2O_4$ (JCPDS 36-0083), respectively. It is true that more rich porous structures will facilitate the adsorption-diffusion of reactive molecules and greatly reduce limitations of interphase mass transfer which can enhance their catalytic activities significantly. As shown in the catalytic performances, the porous MNCO catalyst had much better activity than nonporous one, further indicating the mesoporous structure of oxalate-derived particles play a great important role in the enhancement of catalytic reaction.

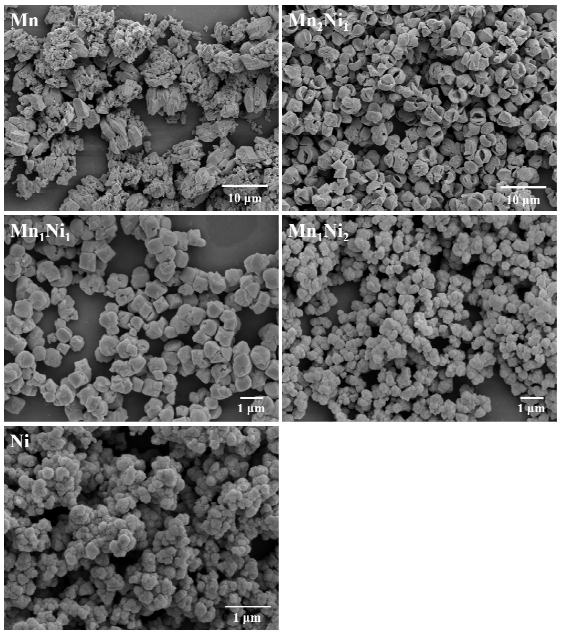

Fig. 6. SEM images of oxalated-derived MNCO catalysts

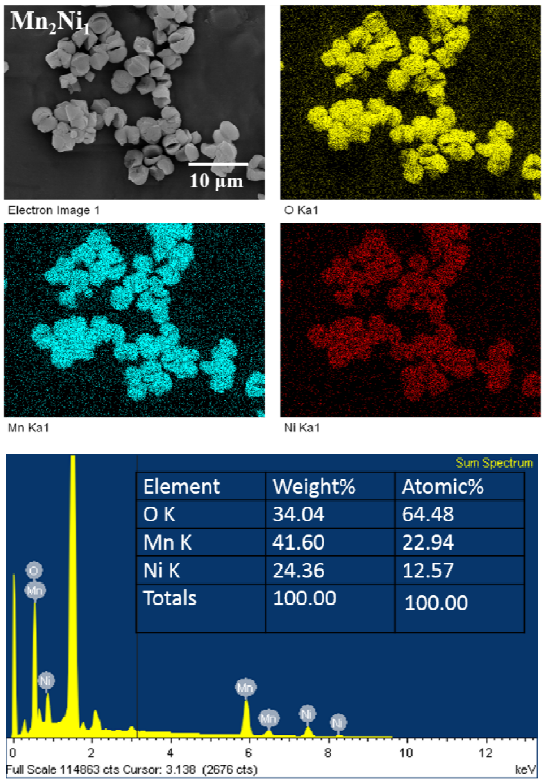

Fig. 7. SEM image, element distribution and EDX data of the oxalate-derived Mn_2Ni_1 mixed oxide

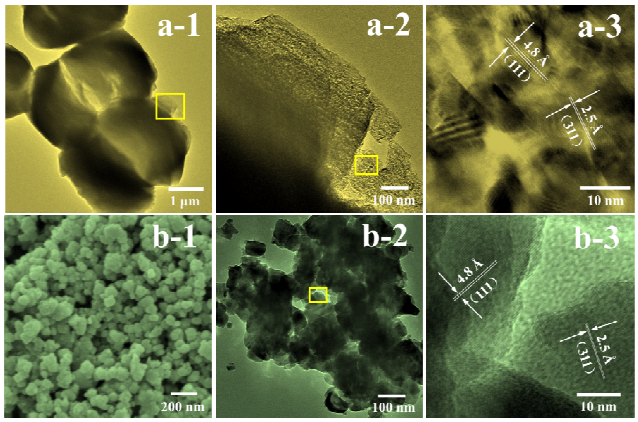

Fig. 8. HRTEM images of the oxalated-derived (a-1, a-2 and a-3) and NaOH-derived (b-1, b-2 and b-3) Mn_2Ni_1 mixed oxide

3.2.3 XPS analysis

To determine the oxidation sates and surface chemical composition of the MNCO catalysts, XPS spectra of Mn 2p, Ni 2p and O 1s are recorded. As shown in Fig. 9, the asymmetrical Mn $2p_{3/2}$ XPS spectra can be deconvoluted into three peaks with a peak-fitting deconvolution method. The binding energies (BE) at 640.7 eV, 641.8 eV and 643.4 eV are assigned to the surface Mn^{2+}, Mn^{3+} and Mn^{4+} species, respectively[32, 33]. Based on the fitting peak area, the content of Mn^{n+} were calculated and the results are summarized in Table 3. With incorporation of Ni species, the population of higher manganese oxidation states (Mn^{3+}, Mn^{4+}) in MNCO sample increased significantly.

Meanwhile, the Ni 2p3/2 spectra of Mn_2Ni_1 mixed oxide and single NiO are represented in Fig. 9 b. Three typical peaks at biding energy (BE)= 854.7, 856. and 861.5 eV were observed, which can be ascribed to the Ni^{2+}, Ni^{3+} and related satellite, respectively[34]. The results show that the composite oxides have a little more Ni^{2+}, which may be contributed to increasing higher oxidation state of manganese (Mn^{3+} or Mn^{4+}). Because of electroneutrality, much more surface bonded oxygen especially adsorbed oxygen species will be generated with development of higher manganese oxidation states. The distribution of surface oxygen species can be figured out by investigating the O 1s XPS spectra. In Fig. 9c, three components were used to fit the asymmetrical O 1s signal: main lattice oxygen at about 529.7 eV, adsorbed oxygen species at 531.2 eV, and adsorbed OH groups/molecular water at 532.1-532.9 eV [35, 36]. The Mn_2Ni_1 sample has more adsorbed oxygen species which is highly correlated with the population of higher metal oxidation state and make a great contribution on catalytic oxidation of VOCs.

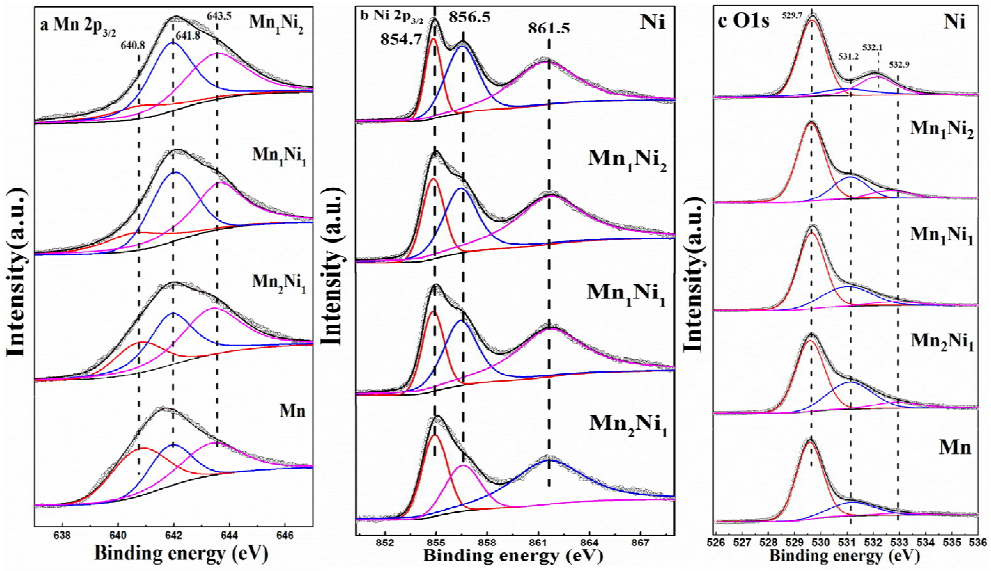

Fig. 9. (a) Mn 2p3/2, (b) Ni 2p, (c) O 1s XPS spectra of oxalate-derived MNCO, single MnO_x and NiO.

Table 3 surface elemental compositions of selected MNCO catalysts

Sample	Mn^{2+} (%)	Mn^{3+} (%)	Mn^{4+} (%)	Ni^{2+} (%)	Ni^{3+} (%)	O_{latt} (%)	**O_{ads} (%)**	O_{sur} (%)
Mn	39.1	25.6	35.3	-	-	72.5	**22.8**	4.6
Mn_2Ni_1	18.2	37.1	44.7	39.6	60.4	57.9	**32.6**	9.5
Mn1Ni1	17.1	39.0	43.9	39.4	60.6	65.2	**29.4**	5.4
Mn1Ni2	13.7	44.4	41.9	37.5	62.5	68.1	**22.4**	9.5
Ni	-	-	-	35.8	64.2	60.4	**16.0**	23.6

3.2.4 H_2-TPR results

H_2-temperature programmed reduction (H_2-TPR) experiments were applied to determine the reducibility of as-prepared MNCO catalysts and the results are represented in Fig. 10. In terms of single manganese oxide, two typical regions of hydrogen consumption in the ranges of 200-300 and 300-450 ºC was observed, ascribed to the reduction sequence of MnO_x to Mn_3O_4 and Mn_3O_4 to MnO respectively [14, 23, 26]. However, there was only one asymmetrical reduction peak in the range of 250-350 ºC for single NiO sample, attributed the possible overlapping reduction process of Ni^{3+} to Ni^{2+} and Ni^{2+} to Ni^0 [37]. However, the reduction of mixed oxide sample is so complex and more than three reduction peaks can be observed. Compared to the reduction patterns of single oxide, the reduction of nickel component becomes difficult (reduction zone transforms to higher temperature) while the reduction of manganese component turns to be more feasible (reduction zone transforms to lower temperature). With the formation of Mn-Ni solid solution, different manganese and nickel ions will coexist in an identical spinel crystal structure. Because of the diverse size of different metal ions (Mn^{2+}=0.091 nm, Mn^{3+}=0.066 nm. Mn^{4+}=0.052 nm, Ni^{2+}=0.069 nm and Ni^{3+}=0.056 nm), a strong synergetic effect among them will be

created ($Mn^{4+}/Mn^{3+}+Ni^{2+} \leftrightarrow Mn^{3+}/Mn^{2+}+Ni^{3+}$) and the activity of related bonded oxygen will be affected significantly. From the TPR results, the reduction of manganese species become more favorable, indicating the incorporation of nickel ions is beneficial for generation of the manganese ions with higher oxidation states then more active oxygen will be formed in the mixed oxide sample. Importantly, a typical reduction peak at about 200 ºC appeared on the Mn_2Ni_1 and Mn_1Ni_1 samples, demonstrating more active oxygen at lower temperature could be used. It turns out that the mixed oxides will perform better which has been shown in catalytic activities. Compared to the nonporous MNCO sample prepared by traditional NaOH co-precipitation method, oxalated-derived MNCO catalyst exhibited a better low temperature reducibility. As displayed in Fig. S1b, there is an obvious reduction peak below 250 ºC on porous Mn_2Ni_1 sample but nothing happened on the nonporous sample. It is suggested that the low temperature reducibility is highly correlated with the activity of surface oxygen species which will enhance the catalytic oxidation activities.

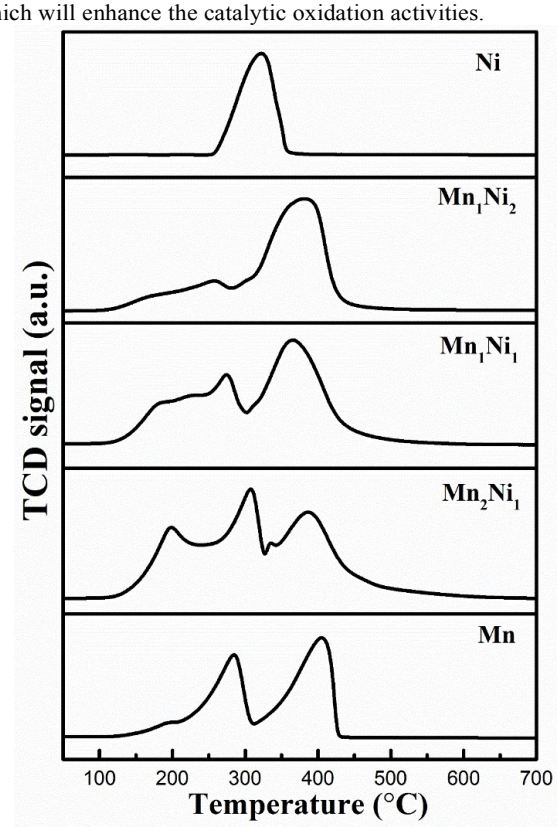

Fig. 10 H_2-TPR profiles of the as-prepared catalysts

4. Important role in catalytic oxidation reaction

4.1 Porous structure

Recently, various efforts have been devoted to studying the correlation between catalytic performances and structural properties such as crystal phases[38, 39], crystal planes[40, 41], morphologies[37, 42, 43] and porous structures[44, 45]. Porous structure, one of the most important structural properties, can not only provide much surface area but also facilitate the adsorption and diffusion of reactant molecules. It is suggested that more active sites will be exposed by developing serious porous structures especially the anomalous pores in small size. In this report, a well-developed porous structure was created by controlling heat treatment of oxalate precursors. During the decomposition of oxalate chains chelated in the corresponding precursors, the release of gaseous H_2O and CO_x will leave behind large amounts of voids and in-situ nanoparticles. From the TEM and BET results, all oxalate-derived MNCO catalysts exhibited rich pore structure and narrow pore size distribution at about 4.0 nm. Compared to the porous MNCO catalyst (Mn_2Ni_1), NaOH-derived particles without porous structure showed much lower catalytic performance for oxidation of gaseous benzene, demonstrating the porous structure is an important factor on the catalytic oxidation.

4.2 Synergistic effect

In most cases, improvement of catalytic oxidation process over single oxide catalysts is limited so that the addition of another component into the single system will be favorable. Generally, three typical methods are used for building synergistic effect in catalysts: doping, making solid solutions and inner-connected composite oxides. The as-prepared MNCO catalysts in this study are all well-crystallized solid solutions with spinel structure, where both manganese and nickel ions are existed in a same crystal structure. A synergistic reduction cycle like $Mn^{4+}/Mn^{3+}+Ni^{2+} \leftrightarrow Mn^{3+}/Mn^{2+}+Ni^{3+}$ can be formed during the surface reaction which can be explained as the synergistic effect in MNCO catalysts. It is well known that both the reduction cycles of $Mn^{2+/3+} \leftrightarrow Mn^{3+/4+}$ and $Ni^{2+} \leftrightarrow Ni^{3+}$ are highly associated with the activation of gaseous oxygen during the catalytic oxidation process. The solid solution oxide provide a desirable situation for making valuable synergistic effect among the different metal ions (Mn^{n+} and Ni^{n+}), which will make a significant promotion on the surface chemical properties of catalysts. However, the mole ratio of metal ions has a great effect on catalytic activities while the MNCO of Mn_2Ni_1 performed best, further indicating a suitable distribution of different metal components should be controlled carefully. From XPS and H_2-TPR analysis, the oxalate-derived Mn_2Ni_1 catalyst showed more adsorbed oxygen species and better reducibility which would make a great contribution on the catalytic reaction. Moreover, it is true that the synergistic effect of different metal ions can also improve the porous structures during the heating process as shown before.

5. Conclusions

A series of novel MNCO catalysts well-developed porous structures were fabricated by s simple oxalate route. The mole ratio of Mn/Ni used in synthetic process significantly affected the physiochemical properties of as-prepared mixed oxides such as morphology, surface area and reducibility. The uniform hierarchical lithops-like Mn_2Ni_1 sample owned a higher surface area of 201.1 m^2g^{-1} and a narrow pore size distribution

(centered at about 4.0 nm). The complete conversion of benzene over this best-performed catalyst can be achieved at as low as 250 ºC and it sustain the complete conversion at 250 ºC for 36 h even under high relative humidity condition. The characterization results revealed that the surface adsorbed oxygen species and redox ability of oxalated-derived Mn_2Ni_1 mixed oxide was significantly promoted by the strong synergistic effect between Mn and Ni species. Therefore, the superior catalytic activity of MNCO catalyst is ascribed to the well-developed porous structure and strong synergistic effect.

Acknowledgements

This work was financially supported by the National Natural Science Foundation of China (No. 51272253; No. 51002154; No. 21401200), the 863 Hi-tech Research and Development Program of China (grant No. 2013AA031801), the Strategic Project of Science and Technology of Chinese Academy of Sciences (No. XDB05050000).

Notes and references

1 R.-J. Huang, Y. Zhang, C. Bozzetti, K.-F. Ho, J.-J. Cao, Y. Han, K. R. Daellenbach, J. G. Slowik, S. M. Platt, F. Canonaco, P. Zotter, R. Wolf, S. M. Pieber, E. A. Bruns, M. Crippa, G. Ciarelli, A. Piazzalunga, M. Schwikowski, G. Abbaszade, J. Schnelle-Kreis, R. Zimmermann, Z. An, S. Szidat, U. Baltensperger, I. E. Haddad and A. S. H. Prevot, *Nature*, 2014, **514**, 218-222.

2 M. Li and L. Zhang, *Environ. Pollut.*, 2014, **189**, 85-86.

3 A. P. Altshuller, *Atmospheric Environment (1967)*, 1983, **17**, 2131-2165.

4 J. Kesselmeier and M. Staudt, *Journal of Atmospheric Chemistry*, 1999, **33**, 23-88.

5 A. P. Jones, *Atmos. Environ.*, 1999, **33**, 4535-4564.

6 J. A. Bernstein, N. Alexis, H. Bacchus, I. L. Bernstein, P. Fritz, E. Horner, N. Li, S. Mason, A. Nel, J. Oullette, K. Reijula, T. Reponen, J. Seltzer, A. Smith and S. M. Tarlo, *Journal of Allergy and Clinical Immunology*, 2008, **121**, 585-591.

7 K. Everaert and J. Baeyens, *Journal of hazardous materials*, 2004, **109**, 113-139.

8 F. I. Khan and A. Kr. Ghoshal, *Journal of Loss Prevention in the Process Industries*, 2000, **13**, 527-545.

9 S. Zuo, Q. Huang and R. Zhou, *Catal. Today*, 2008, **139**, 88-93.

10 Z. Yang, J. Li, H. Zhang, Y. Yang, M. Gong and Y. Chen, *Catalysis Science & Technology*, 2015, **5**, 2358-2365.

11 J. S. Yang, W. Y. Jung, G. D. Lee, S. S. Park, E. D. Jeong, H. G. Kim and S.-S. Hong, *Journal of Industrial and Engineering Chemistry*, 2008, **14**, 779-784.

12 H. C. Genuino, S. Dharmarathna, E. C. Njagi, M. C. Mei and S. L. Suib, *The Journal of Physical Chemistry C*, 2012, **116**, 12066-12078.

13 L. F. Liotta, H. Wu, G. Pantaleo and A. M. Venezia, *Catalysis Science & Technology*, 2013, **3**, 3085-3102.

14 A. R. Gandhe, J. S. Rebello, J. L. Figueiredo and J. B. Fernandes, *Applied Catalysis B: Environmental*, 2007, **72**, 129-135.

15 X. Li, H. Dai, J. Deng, Y. Liu, Z. Zhao, Y. Wang, H. Yang and C. T. Au, *Applied Catalysis A: General*, 2013, **458**, 11-20.

16 B. de Rivas, R. López-Fonseca, C. Jiménez-González and J. I. Gutiérrez-Ortiz, *Chemical Engineering Journal*, 2012, **184**, 184-192.

17 L. F. Liotta, M. Ousmane, G. Di Carlo, G. Pantaleo, G. Deganello, A. Boreave and A. Giroir-Fendler, *Catal. Lett.*, 2008, **127**, 270-276.

18 D. Zhang, Y. Qian, L. Shi, H. Mai, R. Gao, J. Zhang, W. Yu and W. Cao, *Catalysis Communications*, 2012, **26**, 164-168.

19 H. Li, G. Qi, Tana, X. Zhang, W. Li and W. Shen, *Catalysis Science & Technology*, 2011, **1**, 1677.

20 S. Cai, D. Zhang, L. Zhang, L. Huang, H. Li, R. Gao, L. Shi and J. Zhang, *Catalysis Science & Technology*, 2014, **4**, 93-101.

21 B. Shen, Y. Wang, F. Wang and T. Liu, *Chemical Engineering Journal*, 2014, **236**, 171-180.

22 R. Gao, D. Zhang, P. Maitarad, L. Shi, T. Rungrotmongkol, H. Li, J. Zhang and W. Cao, *The Journal of Physical Chemistry C*, 2013, **117**, 10502-10511.

23 W. Tang, X. Wu, S. Li, W. Li and Y. Chen, *Catalysis Communications*, 2014, **56**, 134-138.

24 L. Zhang, L. Shi, L. Huang, J. Zhang, R. Gao and D. Zhang, *ACS Catalysis*, 2014, **4**, 1753-1763.

25 Z. Zhao, Y. Li, T. Bao, G. Wang and T. Muhammad, *Catalysis Communications*, 2014, **46**, 28-31.

26 W. Tang, X. Wu, S. Li, X. Shan, G. Liu and Y. Chen, *Applied Catalysis B: Environmental*, 2015, **162**, 110-121.

27 Y. Yang, J. Huang, S. Wang, S. Deng, B. Wang and G. Yu, *Applied Catalysis B: Environmental*, 2013, **142–143**, 568-578.

28 S. Cai, D. Zhang, L. Shi, J. Xu, L. Zhang, L. Huang, H. Li and J. Zhang, *Nanoscale*, 2014, **6**, 7346-7353.

29 C. He, L. Yue, X. Zhang, P. Li, B. Dou, C. Ma and Z. Hao, *Asia-Pacific Journal of Chemical Engineering*, 2012, **7**, 705-715.

30 Z. Zhu, G. Lu, Z. Zhang, Y. Guo, Y. Guo and Y. Wang, *ACS Catalysis*, 2013, **3**, 1154-1164.

31 M. I. Zaki, A. K. H. Nohman, C. Kappenstein and T. M. Wahdan, *Journal of Materials Chemistry*, 1995, **5**, 1081-1088.

32 Z. Chen, Q. Yang, H. Li, X. Li, L. Wang and S. Chi Tsang, *Journal of Catalysis*, 2010, **276**, 56-65.

33 D. Zhang, L. Zhang, L. Shi, C. Fang, H. Li, R. Gao, L. Huang and J. Zhang, *Nanoscale*, 2013, **5**, 1127-1136.

34 Z. Ren, V. Botu, S. Wang, Y. Meng, W. Song, Y. Guo, R. Ramprasad, S. L. Suib and P. X. Gao, *Angew Chem Int Ed Engl*, 2014, **53**, 7223-7227.

35 L. Yu, G. Diao, F. Ye, M. Sun, J. Zhou, Y. Li and Y. Liu, *Catalysis Letters*, 2011, **141**, 111-119.

36 K. Jirátová, J. Mikulová, J. Klempa, T. Grygar, Z. Bastl and F. Kovanda, *Applied Catalysis A: General*, 2009, **361**, 106-116.

37 G. Bai, H. Dai, J. Deng, Y. Liu and K. Ji, *Catalysis Communications*, 2012, **27**, 148-153.

38 J. Zhang, Y. Li, L. Wang, C. Zhang and H. He, *Catalysis Science & Technology*, 2015, **5**, 2305-2313.
39 Y. Xie, Y. Yu, X. Gong, Y. Guo, Y. Guo, Y. Wang and G. Lu, *CrystEngComm*, 2015, **17**, 3005-3014.
40 L. Hu, Q. Peng and Y. Li, *Journal of the American Chemical Society*, 2008, **130**, 16136-16137.
41 K. Zhou, X. Wang, X. Sun, Q. Peng and Y. Li, *Journal of Catalysis*, 2005, **229**, 206-212.
42 W. Huang and Y. Gao, *Catalysis Science & Technology*, 2014, **4**, 3772-3784.
43 Y. Li and W. Shen, *Chemical Society Reviews*, 2014, **43**, 1543-1574.
44 H. Chen, Y. Yan, Y. Shao and H. Zhang, *RSC Advances*, 2014, **4**, 55202-55209.
45 C. M. A. Parlett, K. Wilson and A. F. Lee, *Chemical Society Reviews*, 2013, **42**, 3876-3893.
46